Small Animal PET Camera Design Based on 2-mm Straw Detectors

Nader N. Shehad, *Member, IEEE,* Athanasios Athanasiades, *Member, IEEE,* Christopher S. Martin, Liang Sun, *Member, IEEE,* and Jeffrey L. Lacy, *Member, IEEE*

***Abstract*–Depth of interaction (DOI) errors in commonly employed crystal detectors cause severe degradation of off-axis resolution in current positron emission tomography (PET) scanners used for small animal or single organ imaging. We propose a PET camera design that uses low cost, easily fabricated, lead-walled straw (LWS) detectors. Photons converted in Pb generate photoelectrons that escape into the straw interior producing an avalanche whose position can be readily measured with high precision. Straws can be of considerable length (up to 50 cm), but small in diameter (2 mm), and can be packed to form scanners with high sensitivity and large fields of view (FOV). The rigorous three-dimensional position encoding eliminates DOI errors encountered in crystal detectors, and provides submillimeter resolution and sensitivity response that is uniform over the full extent of the FOV. We present preliminary results of the operation of a prototype 200-straw module. We then propose a PET scanner design that consists of two rotating trapezoidal detector panels, each panel containing fourteen 200-straw modules (a total of 5600 straws). The FOV has a diameter of 5 cm and extends axially to 15 cm. This unique geometry affords a long field of view, with near constant axial sensitivity of 4.7%, and uniform resolution of 0.9×0.9×1.0 mm^3 maintained over the entire extent of the FOV, as determined in Monte Carlo simulations.**

I. Introduction

While PET imaging is of great utility in the clinical assessment and monitoring of human disease, it is also an extremely powerful tool for the study of fundamental biological processes in living animal models. To date, this utility remains limited by the lack of affordable high-resolution, high-sensitivity small animal PET (SAP) scanners. Commercially successful SAP scanners, listed in Table 1, use crystal-based detectors and both the crystal material itself and micro-fabrication of large numbers of small detector elements contribute significantly to the high ($500,000 - $860,000) cost of these instruments. In addition, crystal-based detectors suffer from narrow axial field-of view (FOV) and also from strong variation in both resolution and sensitivity over this narrow field, all produced by depth-of-interaction (DOI) errors or from design constraints required to avoid them.

We propose a detector technology, based on long *straws* (up to 50 cm) of small diameter (2 mm), that incorporate lead inside their wall, as depicted in Fig. 1. Photons converted in Pb generate energetic electrons that subsequently ionize the gas contained within each straw. Each straw is operated as a proportional detector, with a resistive wire tensioned through its center, serving as the anode electrode.

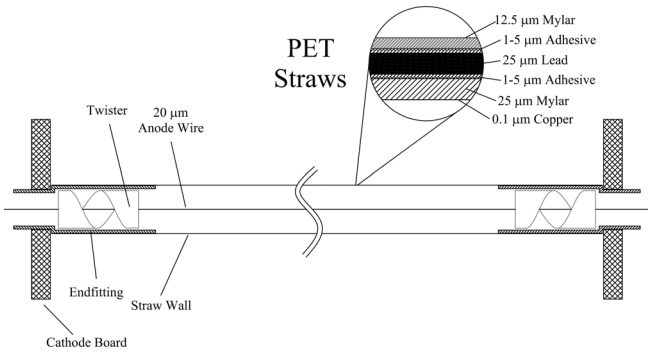

Fig. 1. Lead-walled straw detector for PET imaging.

We then propose development of a SAP scanner that consists of two rotating trapezoidal detector panels, as shown in Fig. 2. Each panel contains fourteen modules, and each module is a grouping of 200 straw detectors. Signals are read out in a manner that provides 3D localization of interacting photons.

We show in Monte Carlo simulations that the proposed detectors and scanner design offer high spatial resolution and

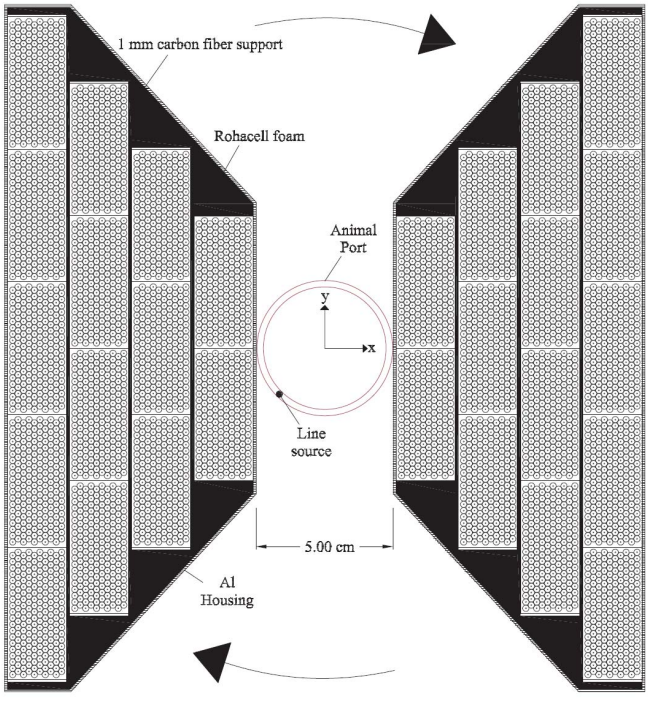

Figure 2: Proposed straw camera.

This work was supported by the NIH under SBIR grant no. RR13482 and RR15993.

All authors are with Proportional Technologies, Inc., Houston, TX 77054 USA (telephone: 713-747-7324, e-mail: jlacy@proportionaltech.com).

sensitivity that are uniform over a Ø 5 cm × 15 cm FOV. By providing precise 3-dimensional location of interacting gamma rays this approach totally eliminates DOI errors, the fundamental limiting factor preventing economical high precision, high resolution crystal based cameras.

Preliminary results of this development have been published in [1].

II. Monte Carlo Simulation of Camera Design

The performance of the proposed straw camera was explored in Monte Carlo simulations, implemented in MCNP4C. The straw camera consisted of two rotating trapezoidal detector panels, as shown in Fig. 2, each containing fourteen 200-straw modules (a total of 5600 straws in both panels). Each straw was 50 cm long, 2 mm in diameter and incorporated a thin layer of lead in its wall (lead thickness discussed below). Two layers of plastic (25 μm and 12.5 μm thick mylar) on either side of the lead layer were also simulated (see Fig. 1). All particle physics available in MCNP4C were utilized, including photoelectric absorption and Compton recoil of photons, and electron creation and interactions, within all straw wall layers and gas volume. Detections were recorded whenever photoelectrons or Compton-electrons escaped into the gas volume, following a photon interaction in the straw wall. Events detected in multiple straws within the same panel were discarded. No energy cut was applied. Cyclic rotation of the modules around their long central axis was also simulated.

A. Reconstructed Image Resolution

Image resolution was predicted for a line source phantom that occupied a large extent of the FOV. A total of 30 1-cm long line sources were simulated, oriented parallel to the y axis, and at a distance of 1 cm from one another, as shown in the reconstructed image of Fig. 3. Finite positron range effects were not simulated. Photons emitted from the source were tracked through each layer of each straw lying within the photon path, until fully absorbed or escaped. Photoelectrons or Compton-electrons generated from photon interactions were in turn tracked inside the detector structure until stopped or escaped. A detection was recorded whenever a photoelectron or Compton-electron entered the gas volume contained within a straw. The x and y coordinates of that detection were identified as the center of the straw; the z coordinate of the detection was the z coordinate of the electron entry point into the gas volume. This coordinate was extraneously perturbed with a Gaussian 2.0 mm FWHM distribution to produce a very conservative simulation of the worst case straw module longitudinal resolution (see section IV on prototype testing). The x, y error in the detection coordinates originated from straw segmentation (2 mm straw diameter). Additionally, a detection could register in a neighboring straw, if the energetic electron were able to escape the original straw wall, and subsequently penetrate the wall of a neighboring straw. The effect of such neighboring-straw detections on image resolution were investigated by varying the thickness of the lead layer inside the wall of each straw.

TABLE 1. COMMERCIALLY AVAILABLE DEDICATED SAP SCANNERS [2-10]

Trade-mark	Manu-facturer	FOV axial (cm) / transaxial (cm)	CFOV Radial Res. (mm)	Average Volumetric Resolution[1] (μL)	CFOV Sensitivity (energy window, keV)	Aver. Sens.[1]	Scatter Fraction[2] (energy window)	Detector	Apprx Price ($)	Approx # Installed
ClearPET Neuro	Raytest	11 / 12.5	1.2	5.1[3]	4.2% (350-650)	3.0%	35% (350-650)	LYSO - LuYAP	860k	4
eXplore Vista DR	General Electric	4.6 / 6	1.4	6.1	4.0% (250-700)	2.1%	28% (250-700)	LGSO/ GSO	700K	20
HIDAC-NanoPET	Oxford Positron Systems	28 / 17	1.1	1.3	1.1%	0.8%	29%	HIDAC multiwire	500k	5
Inveon	Siemens	12.7 / 10	1.6	6.5	7.5% (350-650)	4.0%	6.3% (250-650)	LSO	650k	1[4]
microPET R4	Siemens	7.8 / 10	1.7	15.6	2.25% (250-650)	1.2%	30% (250-750)	LSO	450k	25
microPET Focus 120	Siemens	7.6 / 10	1.6	8.2	7.1% (250-750)	3.5%	27% (250-750)	LSO	650k	25
microPET Focus 220	Siemens	7.6 / 19	1.3	6.0	3.4% (250-750)	1.8%	19% (250-750)	LSO	850k	25
Mosaic	Philips	11.6 / 12.8	2.2	> 20	1.2% (410-665)	0.84%	n/a	GSO	600k	15
X-PET	Gamma Medica	11.8 / 10	1.6	6.7	10%	5.3%	15%	BGO	400k	7
2mm LWS	**PTI**	**30 / 5**	**1.0**	**1.2**	**4.4%**	**4.1%**	**19%**	**LWS**	**325k**	**-**

[1] Averaged over a cylindrical field of view, 5 cm diameter and 7 cm long, [2] All with a mouse phantom, except for ClearPET (with a rat phantom), [3] ClearPET with DOI, [4] First commercial unit will be shipped to University of Wisconsin by the end of 2006.

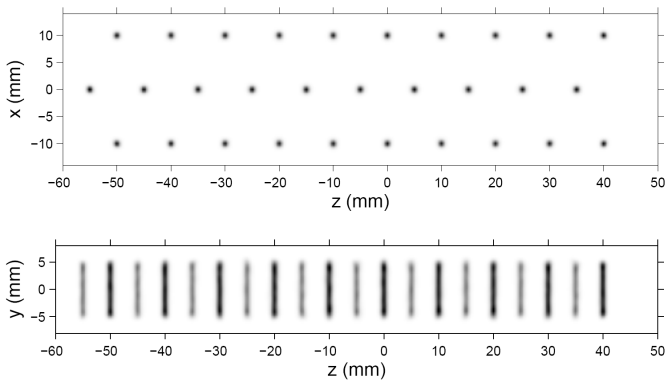

Fig. 3. Reconstructed image of a multi-source phantom, based on a Monte Carlo simulation of the camera design depicted in Fig. 1. top, xz projection, bottom, yz projection.

An image resolution of 1.8×1.8×1.5 mm^3 (FWHM) was obtained using the Monte Carlo (MC) data and a 3D EM-ML image reconstruction method. This set of MC data employed a nominal lead thickness of 25 μm. For this value, approximately one half of the total coincidence rate in the camera involves neighboring-straw detections. Increasing the lead wall thickness to 50 μm resulted in a reconstructed image resolution of 1.4×1.4×1.5 mm^3, clearly a significant improvement on the order of 40% in volumetric resolution. The coincidence fraction involving neighboring-straw detections dropped to 20% for this lead thickness. The effect on camera sensitivity and scatter fraction (see below) was negligible.

Further improvements in image resolution were possible by incorporating resolution modeling to the image reconstruction algorithm. Using a resolution kernel of 1.4×1.4×1.5 mm^3, the resulting reconstructed image resolution was 0.8×0.8×0.9 mm^3 = 0.58 μl. Resolution was highly uniform over the full extent of the phantom, as shown in Fig. 3.

B. *Camera sensitivity*

The sensitivity η of the proposed camera was 4.7%, for a point source in the center of the field of view (FOV). Due to the large axial extent of the camera, the value of η was nearly uniform over a 15 cm long FOV, as shown in Fig. 4. Simulations for 40 cm and 30 cm long cameras are also shown in the figure, indicating the manner by which straw length affected the axial variation of η. The commercially available microPET Focus 120 SAP scanner offers a central FOV sensitivity of 7%, however, the axial extent of that camera is limited to 7.6 cm, significantly less than what is required for imaging a whole rat or even optimally imaging a whole mouse in a single camera position.

The proposed camera offers both increased sensitivity and uniform sensitivity over a 15 cm long FOV. In most practical imaging situations where more than a few cm field of view is required this translates to markedly increased sensitivity and operational convenience. Note that our design can very effectively image even two mice simultaneously, as well as an entire large rat. The radial variation of η was on the order of 26%, as shown in Fig. 5. The sensitivity of cameras consisting of either 9 or 6 modules is also plotted in the figure. Different module arrangements were explored, including rectangular

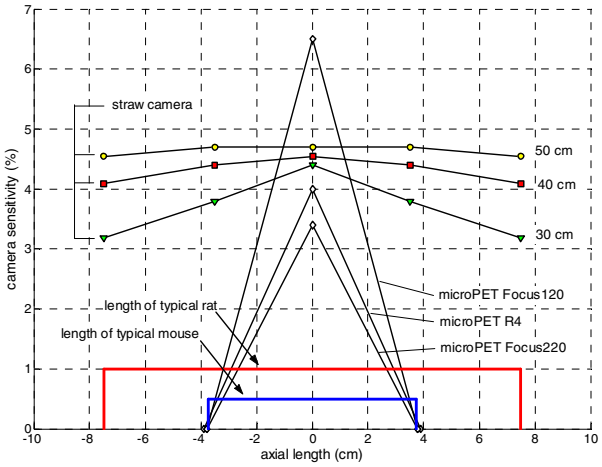

Fig. 4. Sensitivity variation over the axial extent of the proposed camera. Results are presented for different camera (straw) lengths, as indicated. Superimposed is the sensitivity of three commercial PET scanners.

shapes. The 14 module design depicted in was the optimal solution for maximum absolute sensitivity, and radial uniformity.

C. *Scatter fraction*

The scatter fraction (SF), defined as the ratio of scatter to the true+scatter coincidence rate, was 30% for a simulated rat phantom (Ø 5 cm × 15 cm), and 19% for a mouse phantom (Ø 3 cm × 7.5 cm). The SF was estimated by first simulating uniformly distributed positron activity in a cylindrical water-filled phantom. The distance between each line of response (LOR) and the location of the positron annihilation that generated the LOR, was then computed. Those LOR's that did not pass within 1.5 mm from the annihilation point contributed to the SF. The true+scatter coincidence rate was given by $\eta \cdot A$, where A is the positron activity inside the FOV. Fig. 6 shows the distribution of the distance between all LOR's and annihilation locations. The following classes of events did not contribute to the SF: i) events that scattered and were detected

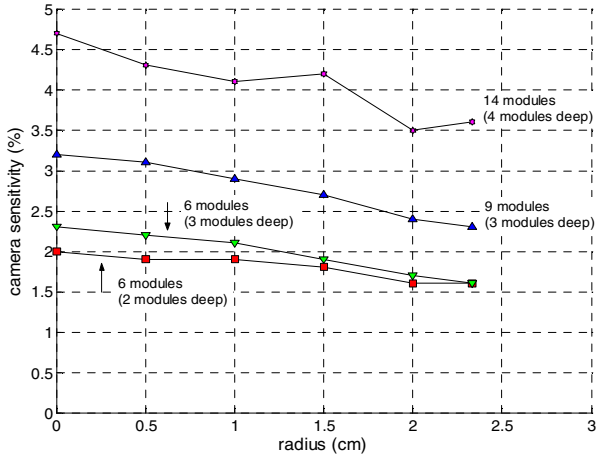

Fig. 5. Sensitivity variation as a function of radius for the proposed camera (14 modules). Cameras incorporating either 6 or 9 modules were also simulated. In the 6-module camera, modules formed either 2×3 or 3×2 arrays. In the 9-module camera, modules were arranged as 2, 3 and 4 in each row.

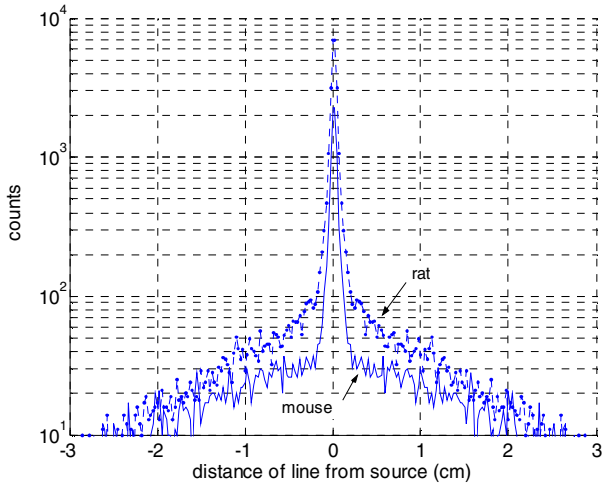

Fig. 6. Distribution of the distance between LOR's and the position of annihilations, inside simulated phantoms of uniform activity. The rat phantom was a water-filled cylinder, of dimensions 5 cm Ø × 15 cm. The mouse phantom has dimensions 3 cm Ø × 7.5 cm The tails surrounding the central peak are an indication of scatter inside the phantom and the detectors.

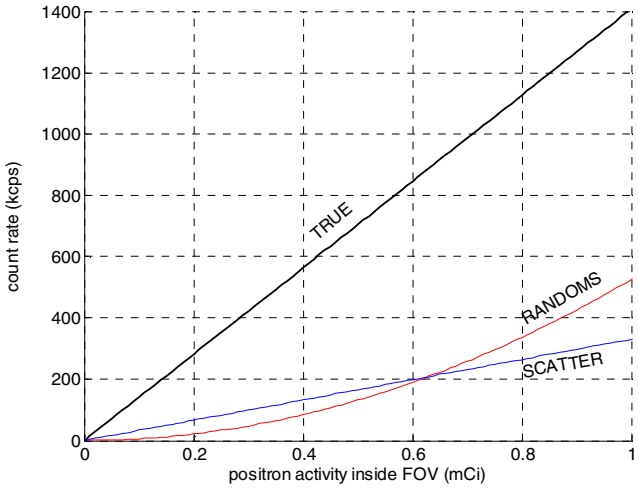

Fig. 7. True, scatter and random coincidence rates in the proposed straw camera. The scatter rate shown is that computed for a mouse phantom (3 cm Ø × 7.5 cm), and was 19% of the true+scatter rate. The randoms rate was computed as explained in the text.

at more than one vertex; ii) events that scattered and were detected at the first vertex only, resulting in a correct LOR; iii) events that scattered such that the corresponding LOR did not cross the FOV.

The SF value reported above includes scatter within the detectors. Simulations have shown that this scatter is about 16%, a reasonable result for a camera of such large axial extent, and no applied energy cut (although some events that scattered would not have sufficient energy to escape the straw wall and be detected). A 30 cm long camera will have a substantially reduced scatter fraction, without a significant loss in sensitivity (see Fig. 4). Also, increasing the thickness of the lead layer to 50 μm, as proposed earlier for improved spatial resolution, has a minimal impact on the scatter fraction (SF=33% for the rat phantom, and 50 cm long camera). The scatter fraction measured in the microPET II scanner [12] is 48% for a rat phantom (Ø 6 cm × 15 cm), and an energy window of 250-750 keV. The scatter fraction attributed solely to the phantom is 31%. The remainder is attributed to scatter in the gantry and environment. The scatter fraction measured for a mouse phantom (Ø 2.5 cm × 7 cm) is 19% (250-750 keV). The value attributed to the phantom only is 4.4%. Thus although the straw system employs no true energy window it is quite competitive regarding scatter fraction.

D. Time resolution & randoms fraction.

We have previously established that the width of the coincidence timing distribution, in a pilot camera made with 2 mm straws, was τ =15 ns [1]. The device consisted of two 20-straw modules, and was operated with a gas mixture of 70% Ar, 29.5% isobutane, and 0.5% freon-13B1. Thus although gas detectors have a reputation for poor time response, by virtue of the small detector diameter and hence small electron drift distance of 1 mm our camera has a quite competitive time resolution which will not impact performance significantly in small animal imaging (see below). The randoms fraction (RF), computed as the ratio of randoms to the true+randoms coincidence rate, was 30% for a source activity of 1 mCi. The randoms rate (R) represented events that did not originate from the same positron annihilation, but randomly happened to be in coincidence, and was computed using the formula, $R=\tau \cdot S^2$, where τ is the coincidence time window, set to 15 ns (98% valid events admitted), and S is the singles rate, defined as the photon detection rate in one of the two detector panels (14 modules). The singles rate was computed as $S=\varepsilon \cdot A$, where ε is the singles efficiency (16%), determined in Monte Carlo simulations, and A is the source activity inside the FOV. The randoms rate is plotted in Fig.7 for a range of activities, along with the true and scatter coincidence rates. Randoms can be quantitatively accounted for by the well known method of collection of a set of data with one of the detector pairs delayed.

III. Prototype Detector Fabrication

A single 200-straw module, shown in Fig. 8, was fabricated and used to evaluate stability of operation, gas gain uniformity, straw decoding and position resolution. The following paragraphs describe some details of the assembly process.

A. Straw Material

Each straw in the module was 2 mm in diameter and 30 cm

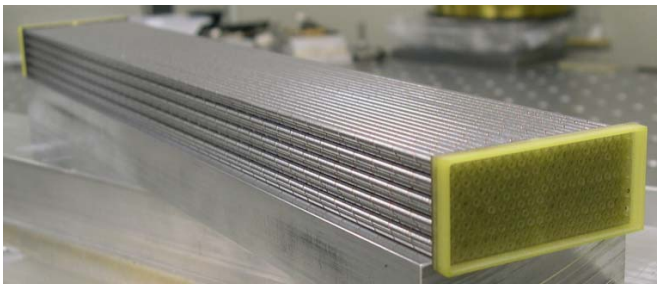

Fig. 8. A partially completed and operated 30 cm long module composed of 200 2 mm straws proving feasibility of 2 mm straw construction techniques.

in length, and incorporated a 25 μm thick layer of lead in its wall. Straws were manufactured using a high speed winding technique in which narrow ribbons of lead-coated plastic film were helically wound around a cylindrical mandrel of precise dimension. Using a custom-made jig support structure to prevent crushing, straws were cut into the desired length. Assembly into honeycomb-like arrays starts by bonding individual rows, which are then stacked vertically. Once a row of straws was assembled, it was then positioned so that straws fit into grooves created by the top of the underlying row. This assembly technique results in very sturdy arrays.

B. End Boards

Fiberglass end-boards, shown in Fig. 9, were designed to attach to the straw array, and serve electrical and structural functions. The cathode board features holes that accommodated all 200 straw fittings, as shown schematically in Fig. 10, and electrically connected all cathodes (straw wall) together. The anode board served as an insulator and anchor for the 200 tensioned anode wires (10 μm resistance wire). The two boards, when mated together, formed an airtight chamber that distributed gas from a single entry port to the 200 straws.

Once assembly was complete, the detector module underwent a series of quality assurance tests, including wire resistance and voltage stability measurements, to ensure proper operation.

C. Electronics

The detector readout was divided up into two stages: front-end and digitization electronics. Front-end electronics consisted of two printed-circuit boards, one on each end of a 100-straw array, designed in-house and manufactured by Proto Circuits (Fort Lauderdale, FL). Each board incorporated three current amplifiers, one on each end of a delay line, where anode wires terminated, and a cathode amplifier used for triggering the digitization system

The delay line was used for straw decoding, within two arrays of 10×10 straws. On one end of the array, all straws within a row were tied together; on the other end, straws were tied together within columns. Each of the 10 columns (rows) were then connected into taps of the delay line, which was read on both ends by current sensitive amplifiers. The relative time difference between the signals on the two ends of the delay line was then used to determine which column (row) an event occurred in. By combining this information with the longitudinal position measured using charge division, a full 3D position was obtained for each detected event.

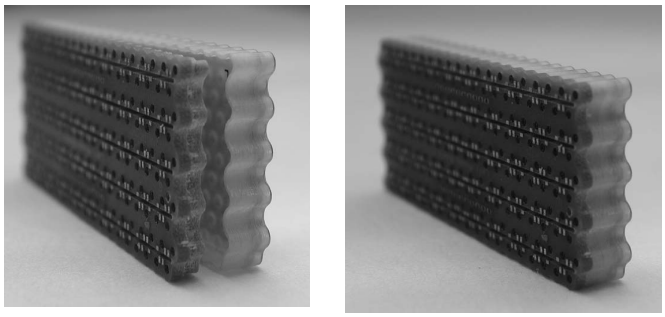

Fig. 9. *left*, Anode and cathode board separately. *right*, Anode and cathode boards mated together forming gas-tight cavity.

Anode and cathode signals were sent to a proprietary digitization system, manufactured by A&D Precision Co. (Newton, MA). The system included 12-bit charge-integrating ADCs to digitize anode signals, as well as a discriminator to trigger the system based on the cathode signal. Once digitized, data were formed into Ethernet packets and sent to a host computer via a gigabit switch. Control software written in C++ was used to acquire the data and store it into files for analysis with MATLAB.

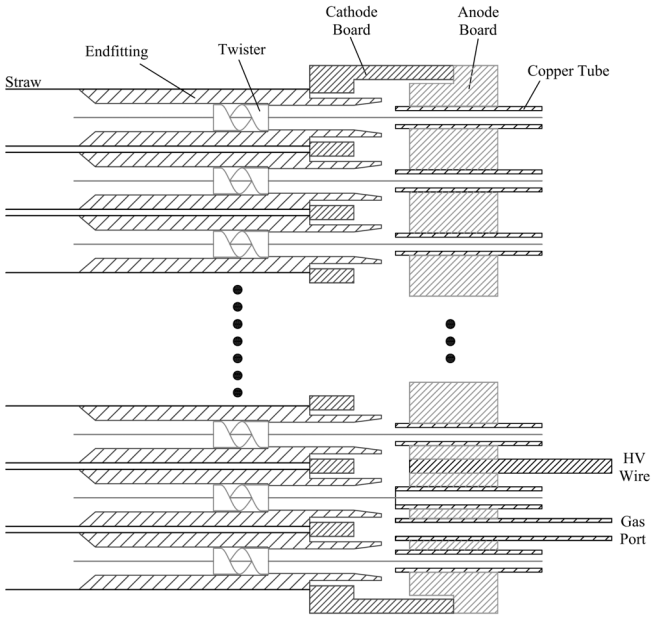

Fig. 10. Cross-section of end board assembly.

IV. Prototype Detector Testing

A. Longitudinal Position Resolution

Longitudinal position was measured using a charge (current) division method [11]. For each event detected in the straw, a current is injected in the anode wire and splits in proportion to the distance from the end of the straw, resulting in a signal on each end (A & B). This current split is determined only by the resistance of the anode wire and is rigorously proportional to the longitudinal position.

Preliminary studies investigated a single 30 cm LWS straw detector with a 10 μm anode wire. Resolution was measured using a narrowly collimated single photon-emitting source (^{99m}Tc). This low energy source is detected with low efficiency, but it has been previously shown that the spatial response to such a source is indistinguishable from that for 511 keV. The source was collimated with a lead shield having a slit width of 0.5 mm. Fig. 11 shows the interaction peaks obtained. The mean resolution was 1.55 mm (FWHM).

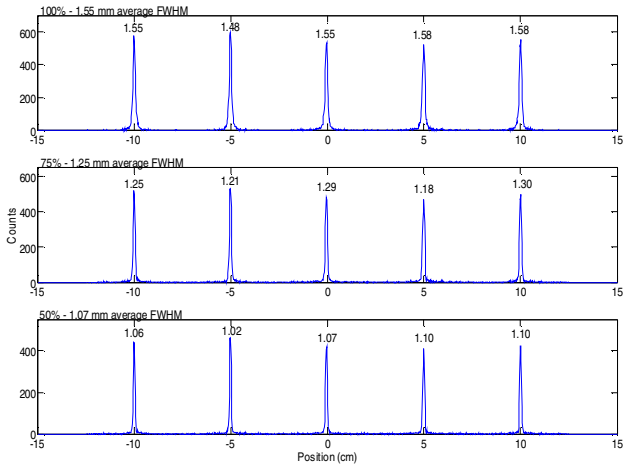

Fig. 11. Five resolution peaks along the length of a single 30 cm long straw detector, showing that spatial resolution improves by rejecting high amplitude events. From top to bottom, resolution plots include 100%, 75%, and 50% of the total data respectively.

At high signal amplitudes, two distinct position peaks exist for each position due to the nature of the charge deposition inside the straw. Photoelectrons emitted from the wall perpendicular to the straw make a short path across the straw before being absorbed by the far wall. On the other hand, oblique electrons travel a much longer distance in the gas before being absorbed in the wall and thus produce a long track depositing much more energy and producing a larger signal. Oblique electrons correlating with high amplitude signals produce more measurement error than perpendicularly emitted photoelectrons and in fact produce a clear splitting in position measurement depending upon the two choices of inclination. A simple amplitude cut excluding the largest amplitudes can be employed to improve detector spatial resolution, with a tradeoff of lower sensitivity. With a 50% cut in sensitivity resolution can be improved from 1.55 mm to under 1.1 mm, as shown in Fig. 11, while with a modest 25% loss of events resolution improves to 1.25 mm.

The z-axis resolution of the 200-straw module was also investigated with a collimated ^{99m}Tc source. Fig. 12 shows the spectrum of interaction locations. The linearity of the peaks is near perfect. The mean full-width-at-half-maximum (FWHM) of the peaks was 3 mm, about a factor of 2 higher than that measured in the single straw, a result of the poor electromagnetic shielding of the module in this initial evaluation. Improved shielding is expected to both produce expected 1.5 mm resolution as well as improve the straw decoding precision.

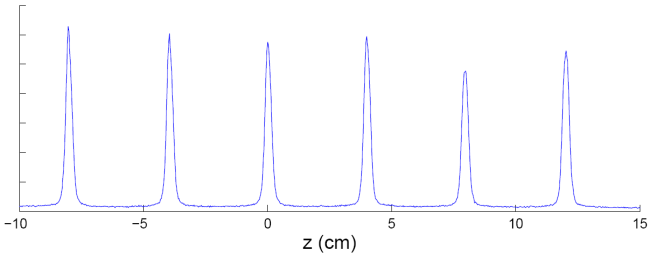

Fig. 12. Position spectra in the $z\psi$direction, collected in the prototype 200-straw module, using a collimated ^{99m}Tc source.

B. *Straw Decoding*

Fig. 13 shows the correlation between the time of arrival of signals, and the corresponding longitudinal location of photon interactions, during a flood irradiation of the 200-straw module. Events are clearly grouped into 10 bands, corresponding to the ten columns in the straw array. A similar plot can be constructed for the 10 rows in the array.

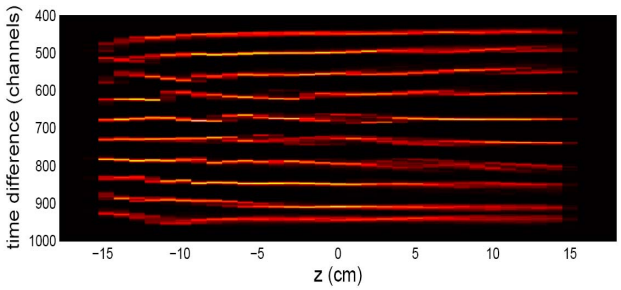

Fig. 13. Correlation between the timing of signals and the corresponding location of photon interactions along the length of the 200-straw module, under uniform irradiation. Each band represents events from one of the ten columns making up the detector module.

V. Conclusion

By allowing detectors to be placed almost in contact with the subject animal, as opposed to the 10 cm or more separation required in crystal systems to avoid DOI blurring, very high sensitivity is achieved with small detector count. This fundamentally new approach provides a greatly expanded uniform high sensitivity FOV allowing imaging time to be reduced by as much as 4 – 6 fold. At the same time simulations indicate that a completely uniform image resolution of 1.0 mm FWHM and 1.2 µL volumetric spatial resolution can be achieved over the entire field of view (Ø 5 cm × 15 cm). Even over a much smaller field of Ø 5 cm × 7 cm, the leading commercial systems produce an average volumetric resolution of no better than 6 µL (see Table 1).

This improved resolution will afford far more effective imaging of mouse models of human disease by far the most significant application of SAP. The close proximity of LWS detectors affords reduction of detector readout module count from 168 used in the microPET Focus 220 for example, to 28 LWS modules, cutting the electronic channel requirements by a striking factor of six. The combined elimination of costly crystals and ~6 fold reduction of electronics will provide a quantum reduction in cost allowing far more facilities to participate in molecular imaging research employing the powerful PET technique and likely greatly expand the instrumentation market.

Finally it is important to note that there are promising human single organ imaging applications for the LWS technology. One of the more promising is a dedicated breast imaging device in which again proximity of placement of detectors produces high sensitivity. Another promising application being explored is brain imaging. The proposed design is thus a very good entry level development which

could lead to diagnostic devices with applicability to very important human imaging applications.

REFERENCES

[1] N. N. Shehad, C. S. Martin, and J. L. Lacy, "Ultra-High Resolution PET Detector Using Lead Walled Straws", IEEE Nuclear Science Symposium Conference Record, vol. 3, pp. 1839-1843, 10-16 Nov. 2002.

[2] K Ziemons, E Auffray, R Barbier et al., "The ClearPET™ project: development of a 2nd generation high-performance small animal PET scanner", Nuclear Instruments and Methods in Physics Research Section A, Vol. 537, pp. 307-311, 2005.

[3] Y Wang, J Seidel, B M W Tsui et al., "Performance Evaluation of the GE Healthcare eXplore VISTA Dual-Ring Small-Animal PET Scanner", J. Nuclear Medicine, vol. 47, pp. 1891-1900, 2006.

[4] J Missimer et al., "Performance evaluation of the 16-module quad-HIDAC small animal PET camera", Phys. Med. Biol. Vol. 49, pp. 2069-2081, 2004.

[5] B Kemp, M Lenox, D Newport et al., "Performance measurements of the Siemens Inveon small animal PET scanner", IEEE Nuclear Science Symposium Conference Record, 29 Oct. – 4 Nov., 2006.

[6] C Knoess, S Siegel, A Smith et al., "Performance evaluation of the microPET R4 PET scanner for rodents", Eur J Nucl Med Mol Imaging, Vol. 30 (5), pp. 737-747, 2003.

[7] R Laforest, D Longford, S Siegel et al., "Performance evaluation of the microPET Focus F120", IEEE Nuclear Science Symposium Conference Record, vol. 5, pp. 2965-2969, 16-22 Oct. 2004.

[8] Y Tai, A Ruangma, D Rowland et al., "Performance evaluation of the microPET Focus: a third-generation microPET scanner dedicated to animal imaging", J Nucl Med, Vol. 46, pp. 455-463, 2005.

[9] M Larobina, A Brunetti and M Salvatore , "Small animal PET: a review of commercially available imaging systems", Current Medical Imaging Reviews, Vol. 2, pp. 187-192, 2006.

[10] Y Zhang, W Wong, H Baghaei et al., "Performance evaluation of the low-cost high-sensitivity rodent research PET (RRPET) camera using Monte Carlo simulations", IEEE Nuclear Science Symposium Conference Record, vol. 5, pp. 2514-2518, 23-29 Oct. 2005.

[11] V. Radeka and P. Rehak, "Charge dividing mechanism on resistive electrode in position-sensitive detectors," *IEEE Trans. Nuc. Sci.*, vol. NS-26, no. 1, pp. 73–80, 1979.

[12] Yang Y, Cherry SR. "Observations Regarding Scatter Fraction and NEC Measurements for Small Animal PET," Nuclear Science Symposium Conference Record, vol. 6, pp. 3906-3910, 16-22 Oct. 2004.